A SECOND ORDER CONTROL-VOLUME FINITE-ELEMENT LEAST-SQUARES STRATEGY FOR SIMULATING DIFFUSION IN STRONGLY ANISOTROPIC MEDIA [*1)]

Jayantha Pasdunkorale A.
(*Department of Mathematics, University of Ruhuna, Matara, Sri Lanka 81000*)

Ian W. Turner
(*School of Mathematical Sciences, Queensland University of Technology, Brisbane, Australia 4001*)

Abstract

An unstructured mesh finite volume discretisation method for simulating diffusion in anisotropic media in two-dimensional space is discussed. This technique is considered as an extension of the fully implicit hybrid control-volume finite-element method and it retains the local continuity of the flux at the control volume faces. A least squares function reconstruction technique together with a new flux decomposition strategy is used to obtain an accurate flux approximation at the control volume face, ensuring that the overall accuracy of the spatial discretisation maintains second order. This paper highlights that the new technique coincides with the traditional shape function technique when the correction term is neglected and that it significantly increases the accuracy of the previous linear scheme on coarse meshes when applied to media that exhibit very strong to extreme anisotropy ratios. It is concluded that the method can be used on both regular and irregular meshes, and appears independent of the mesh quality.

Mathematics subject classification: 74S10, 76M12, 74S05, 76M10.
Key words: Error correction term, Shape Functions, Gradient Reconstruction, Flux Approximation.

1. Introduction

An accurate approximation of the flux at the control volume face is one of the challenges in finite volume discretisation techniques [1, 2] for simulating transport in highly anisotropic media on arbitrary shaped meshes [3, 4, 5, 6, 7, 8, 9]. In the past the hybrid control-volume finite-element method has been used to approximate the necessary fluxes [10, 11, 12, 13], where it has been shown that the use of very fine meshes produces accurate results, however the computational cost is very high, especially for problems in three dimensions [10]. On the other hand this technique fails to provide accurate results on coarse meshes for strongly orthotropic media [13].

This work builds upon the finite volume flux decomposition technique proposed in [9, 14] and seeks to resolve the problems associated with using that scheme under extreme anisotropy ratios, whereby divergence was observed in the iterative solution of the underlying linear system. It was concluded in that work that the main difficulty arose due to the explicit treatment of the cross-diffusion component of the flux, which in some instances of strong anisotropy carries with it the most important contribution of the entire flux. The key factor in resolving this issue is to recover a proportion of this cross-diffusion term in an implicit manner.

One notes that the hybrid (control volume finite element - CVFE) scheme [9, 10, 12, 13] naturally treats the implicitness of the cross-diffusion term via use of the shape functions. Furthermore, this scheme has performed accurately and efficiently (in terms of overall computational overheads) for a variety of isotropic diffusion problems and diffusion problems involving relatively small anisotropy ratios. Unfortunately, the CVFE scheme fails to provide accurate results on coarse meshes when it is used to simulate diffusion in media that exhibit strong to extreme anisotropy ratios. This downfall of CVFE method provides the motivation for this research. It seems reasonable to try improving the accuracy of this scheme using some of the innovative ideas proposed in [9], especially since the hybrid method is straightforward to implement and finds application in a wide range of problems resolved using finite-volume finite-element paradigms. In this work a hybrid scheme is derived that uses a weighted least squares function reconstruction technique to increases the linear accuracy of the scheme summarised in [9] to second order accuracy. The overall appearance of the new hybrid scheme retains the previous linear shape function component of the flux term and includes an explicitly treated correction term that utilises locally estimated derivatives to improve the order of the flux approximation. The attraction of the new scheme is twofold. Firstly, if the correction term is neglected the scheme is identical to the previously proposed linear hybrid scheme, thus enabling it to be accommodated easily into existing codes. Secondly, the cost of estimating the correction term is not overly demanding in terms of computational cost since most of the required terms utilize matrices whose coefficients involve only geometrical mesh properties, which can be decomposed and stored during the initialisation of the code and used thereafter during processing. Most importantly, the new scheme provides the appropriate amount of implicitness to the cross-diffusional component of the flux to overcome the problems reported in [14] for extreme anisotropy ratios. The new scheme works well and has provided accurate simulation results for a wide range of benchmark problems tested, the most important of which are reported here in Section 3.

For anisotropic transport problems, the flux term is given by $\mathbf{q} = -K\nabla\phi$ where $K = \begin{pmatrix} k_{xx} & k_{xy} \\ k_{yx} & k_{yy} \end{pmatrix}$. This situation arises in problems such as heat and mass transfer during drying processes, groundwater flow, atmospheric dispersion, heat conduction in solar power collector plates, microwave and convective heating of hygroscopic materials, thermo-elastic stresses and displacements of anisotropic materials, and manufacturing of composite materials [10, 15, 16, 17, 18, 19, 20, 21].

In this work the following two dimensional unsteady anisotropic diffusion equation for a finite rectangular domain $\Omega = [0, L] \times [0, M]$ is considered.

$$\frac{\partial \psi}{\partial t} - \nabla.(K\nabla\phi) = 0 \quad \text{on} \quad \Omega \quad \text{for} \quad 0 < t \leq T < \infty \tag{1}$$

where ψ is a function of ϕ. The boundary conditions and initial condition are defined as follows:

$$-(K\nabla\phi).\mathbf{n}_b = h(\phi - \phi_s) \quad \text{on} \quad \partial\Omega \quad \text{for} \quad 0 < t \leq T < \infty$$

$$\phi(x, y, 0) = F(x, y) \quad \text{in} \quad \Omega$$

where $\mathbf{n}_b$ is the outward unit normal vector at the boundary $\partial\Omega$ and ϕ_s is a constant associated with the boundary conditions.

2. Finite Volume Discretisation

The finite volume discretisation [1, 2, 13] of the diffusion Eq. (1) over the control volume

δV_P (see Fig. 1) for the time interval $(n\delta t, \overline{n+1}\delta t)$ leads to the following:

$$\delta V_P(\psi_P^{(n+1)} - \psi_P^{(n)}) - \delta t \sum_{k=1}^{N_p} \{\lambda(K\nabla\phi)_{F_k}^{(n)} + (1-\lambda)(K\nabla\phi)_{F_k}^{(n+1)}\}.\hat{\mathbf{n}}_{\mathbf{k}}A_k \simeq 0, \qquad (2)$$

where N_p is the number of control volume faces. For example, in Fig. 1, $A_k = ER$ represents the kth control volume face, which has outward unit normal vector $\hat{\mathbf{n}}_{\mathbf{k}}$, and there are twelve faces in total for the control volume shown. $\lambda = 1$ for an explicit scheme, $\lambda = 0$ for a fully implicit scheme and $0 < \lambda < 1$ for an intermediate scheme.

It should be noted that because the mid-point rule has been emloyed to approximate the line integral during the discretisation in space, the approximation (2) remains second order provided that the term $(K\nabla\phi).\hat{\mathbf{n}}_{\mathbf{k}}$ is known exactly at the center of the control volume face [22]. Therefore, the accurate approximation of this term is crucial if the finite volume scheme is to retain second order and is precisely the topic deliberated in the next section.

2.1 High Order Flux Approximation at CV Face

To approximate $(K\nabla\phi)_{F_k}.\hat{\mathbf{n}}_{\mathbf{k}}$ the following strategy is used, refer to Fig. 1. Assume that the gradient $\nabla\phi$ at the control volume face at $\mathbf{x}_F$ can be written as

$$\nabla\phi = \alpha(\mathbf{x}_F)\mathbf{i} + \beta(\mathbf{x}_F)\mathbf{j} \qquad (3)$$

where the vector $\mathbf{x}_F$ represents the point F, and the functions α and β are to be estimated. It should be noted that the point F is a representative point for the face ER. The tests performed here were carried out either using the midpoint (M) of the face or the center of the triangle (E) instead of the point F. Note however that the use of any point other than E carries with it substantial computational overhead, which will be elaborated on later in the text.

Consider the Taylor expansion of the function ϕ :

$$\phi(\mathbf{x}_F + \delta\mathbf{x}) = \sum_{k=0}^{m} \frac{1}{k!}(\delta\mathbf{x}.\nabla)^k \phi(\mathbf{x}_F) + R \qquad (4)$$

where the remainder R has the *Lagrange form,* and

$$R = \frac{1}{(m+1)!}(\delta\mathbf{x}.\nabla)^{(m+1)}\phi(\mathbf{x}_F + \theta\delta\mathbf{x}); \quad 0 \le \theta \le 1.$$

One can substitute the vectors $\delta\mathbf{l}$, $\delta\mathbf{p}$ or $\delta\mathbf{n}$ for $\delta\mathbf{x}$ in the above equation to obtain the function values at the points L, P or N respectively. For example, $\phi_p = \phi(\mathbf{x}_F + \delta\mathbf{p})$. Hence, after subtraction of the appropriate equations and assuming that remainder terms give negligible contribution, the following expressions for $(\nabla\phi)_F.\mathbf{n}$ and $(\nabla\phi)_F.\mathbf{p}$ can be obtained:

$$(\nabla\phi)_F.\mathbf{n} \simeq \phi_L - \phi_P - \epsilon_{pl} \qquad (5)$$

and

$$(\nabla\phi)_F.\mathbf{p} \simeq \phi_L - \phi_N - \epsilon_{nl} \qquad (6)$$

where, for example,

$$\epsilon_{pl} \simeq \sum_{i=2}^{m} \frac{1}{i!}\{(\delta\mathbf{l}.\nabla)^i - (\delta\mathbf{p}.\nabla)^i\}\phi(\mathbf{x}_F), \qquad (7)$$

$$\mathbf{n} = [n_x, n_y]^T, \quad \mathbf{p} = [p_x, p_y]^T,$$

and $m = 2$ or 3 gives second or third order approximations respectively.

Using Eq. (3) the above equations can be written in matrix form as follows:

$$\Lambda(\nabla\phi)_F \simeq d\underline{\phi} - \underline{c} \text{ or } (\nabla\phi)_F \simeq \Lambda^{-1}d\underline{\phi} - \Lambda^{-1}\underline{c}$$

where

$$\Lambda = \left[\begin{array}{cc} n_x & n_y \\ p_x & p_y \end{array}\right], \quad d\underline{\phi} = \left[\begin{array}{c} \phi_L - \phi_P \\ \phi_L - \phi_N \end{array}\right], \text{ and } \underline{c} = \left[\begin{array}{c} \epsilon_{pl} \\ \epsilon_{nl} \end{array}\right].$$

Note that the matrix Λ is non-singular for non-degenerate triangles and

$$\Lambda^{-1}d\underline{\phi} = \frac{1}{2A}\left(\left[\begin{array}{c} -l_y \\ l_x \end{array}\right]\phi_L + \left[\begin{array}{c} n_y \\ -n_x \end{array}\right]\phi_N + \left[\begin{array}{c} -p_y \\ p_x \end{array}\right]\phi_P\right)$$

where the magnitude of $A = \frac{1}{2}(n_x p_y - n_y p_x)$ is the area of the triangle LNP.

Therefore an expression for the gradient at point F can be written, in terms of usual Lagrangian shape functions, as

$$(\nabla\phi)_F = \sum_{r=L,N,P} (\nabla M_r)\phi_r - \underline{\epsilon}_F$$

with the correction term $\underline{\epsilon}_F = \Lambda^{-1}\underline{c}$ and the M_r's are linear shape functions for the triangle LNP [10, 12], having the properties

$$\sum_{r=L,N,P} M_r = 1 \text{ and } \sum_{r=L,N,P} (\nabla M_r) = 0.$$

Thus, the flux at the point F can be written as

$$(K\nabla\phi).\hat{\mathbf{n}}_{\mathbf{k}} = \sum_{r=L,N,P} (\nabla M_r).(K^T\hat{\mathbf{n}}_{\mathbf{k}})\phi_r - \underline{\epsilon}_F.(K^T\hat{\mathbf{n}}_{\mathbf{k}}). \tag{8}$$

One can see that this expression coincides with the hybrid method discussed in [12, 13] when the last term is ignored.

Using $\lambda = 0$ in Eq. (2) and assuming that $\psi = \gamma\phi$ for the test problem under investigation here, the following implicit discretisation of the diffusion Eq. (1) can be obtained by substituting the flux approximation given by Eq. (8):

$$\gamma\delta V_P\phi_P^{(n+1)} - \delta t \sum_{k=1}^{N_p} \sum_{r_k=L_k,N_k,P} (\nabla M_{r_k}).(K^T\hat{\mathbf{n}}_{\mathbf{k}})A_k\,\phi_{r_k}^{(n+1)}$$
$$\simeq \gamma\delta V_P\phi_P^{(n)} - \delta t \sum_{k=1}^{N_p} \underline{\epsilon}_{F_k}.(K^T\hat{\mathbf{n}}_{\mathbf{k}})A_k \tag{9}$$

This equation provides a system of equations in the form

$$L\underline{\phi}^{(n+1)} = \underline{b}(\underline{\phi}^{(n)}) - \underline{\epsilon} \tag{10}$$

when every node in the mesh is visited and the matrix L is identical to the system matrix obtained for the hybrid technique [12, 13].

To complete the flux approximation, the term $\underline{\epsilon}_F$, which depends on the derivatives of the function at the point F, must be found. The least squares function reconstruction technique is used to estimate the required derivatives. This strategy is discussed by the authors elsewhere [14] and is repeated here in section 2.2 for completeness.

The estimation of the correction term carries with it an additional computational cost when compared to the traditional CVFE scheme and this issue will be discussed in the section 2.2. However, this computational cost can be reduced by using coarser mehses for the technique discussed here than the meshes needed to obtain the same accuracy when the hybrid schemes are used. Note also that the term $\underline{\epsilon}$ is treated explicitly because the derivatives of the function at $(n+1)$th time step is not available.

2.1.1 Treatment of Boundary Conditions

At the boundary control volumes (see again Fig. 3), the value of the function at the boundary point P is assumed to be the same as that of the boundary surfaces and all discrete quantities are calculated there. If a control volume face coincides with a boundary then the above equations are altered by setting the flux through that face equal to the boundary flux, evaluated at point P, multiplied by the length of the boundary control volume face. At a boundary control volume the discretised equations will take the following form:

$$
\gamma \delta V_P \phi_P^{(n+1)} - \delta t \sum_{k=1}^{N_p} \sum_{r_k = L_k, N_k, P} (\nabla M_{r_k}).(K^T \hat{\mathbf{n}}_{\mathbf{k}}) A_k \, \phi_{r_k}^{(n+1)}
$$
$$
- \sum_{b=1}^{N_b} h_b (\phi_b - \phi_P^{(n+1)}) A_b \simeq \gamma \delta V_P \phi_P^{(n)} - \delta t \sum_{k=1}^{N_p} \underline{\epsilon}_{F_k}.(K^T \hat{\mathbf{n}}_{\mathbf{k}}) A_k
$$
(11)

where N_b is the number of boundary control volume faces.

2.2 Improved least squares function reconstruction

Consider the truncated Taylor expansion of the function ϕ:

$$
\phi(\underline{\mathbf{x}}_F + \delta \underline{\mathbf{x}}_j) \simeq \sum_{d=0}^{m} \frac{1}{d!} \left[(\delta \underline{\mathbf{x}}_j.\nabla)^d \phi \right]_{\mathbf{x}_F}.
$$
(12)

Writing Eq. (4) for each node, $j = 1, 2, ..., r$, see Fig. 2 for the nodes indicated by small circles, connected to the point F, the following over-determined system of equations is obtained, (for $m = 3$):

$$
\begin{pmatrix}
1 & \Delta x_1 & \Delta y_1 & ... & \frac{\Delta x_1 \Delta y_1^2}{2} \\
1 & \Delta x_2 & \Delta y_2 & ... & \frac{\Delta x_2 \Delta y_2^2}{2} \\
... & ... & & ... & \\
... & ... & & ... & \\
... & ... & & ... & \\
1 & \Delta x_r & \Delta y_r & ... & \frac{\Delta x_r \Delta y_r^2}{2}
\end{pmatrix}
\begin{pmatrix}
\phi_F \\
\frac{\partial \phi}{\partial x}_F \\
\frac{\partial \phi}{\partial y}_F \\
. \\
. \\
\frac{\partial^3 \phi}{\partial x \partial y^2}_F
\end{pmatrix}
=
\begin{pmatrix}
\phi_1 \\
\phi_2 \\
. \\
. \\
. \\
\phi_r
\end{pmatrix}
$$
(13)

which can be written as
$$
A\mathbf{X} = \mathbf{B}.
$$

The components that minimise $||A\mathbf{X} - \mathbf{B}||^2$ in the least squares sense with respect to a weighted inner product on $\mathbb{R}^r$ can be determined by multiplying the above system by $W_{r \times r} = Diag(w_j)$ and A^T, to arrive at the normal equations

$$
(A^T W A) \, \mathbf{X} = (A^T W \mathbf{B}).
$$
(14)

At a boundary control volume face, see Fig. 3, an equation related to the boundary conditions is added to the above system. For example, for the face F shown in Fig. 3, the equation,

$$
k_{xx} \frac{\partial \phi}{\partial x}_F + k_{xy} \frac{\partial \phi}{\partial y}_F = h_w (\phi_F - \phi_w),
$$

$$\text{or} \quad h_w \phi_F - k_{xx} \frac{\partial \phi}{\partial x}\bigg|_F - k_{xy} \frac{\partial \phi}{\partial y}\bigg|_F = h_w \phi_w,$$

is also inserted to the system of equations given by Eq. (13).

Note that the weight coefficients, w_j's are chosen so that more importance is given to the directions that are the closest neighbours of the point F as opposed to the nodes that are further away from the point F, and $w_j = ||\delta \underline{\mathbf{x}}_j||^{-c}$ for $c = 0, 1,$ or 2 is used here. Solutions of the above weighted least squares problem estimate the function value and the first, second and third derivatives accurately at the point F on the control volume face. Therefore the term $\underline{\epsilon}_F$ required for Eq. (8) can be approximated.

It should be noted that the technique discussed here estimates the function value on the control volume face with high accuracy. The typical least-squares gradient reconstruction technique discussed in [9, 23, 24, 25] approximates only the derivatives of the function.

There is an additional computational cost involved with this least squares function reconstruction required to estimate the correction term of the finite volume scheme discussed in the above section. However, the matrix in Eq. (13), which depends only on geometrical properties, can be decomposed and stored once, at the initial time step and used subsequently to solve that system during the simulation. On the other hand, the fact that this CVFE-LS scheme can enable accurate results on coarse meshes provides an advantage over the traditional hybrid techniques, because they need fine meshes to obtain the same level of accuracy.

2.3 Selection of point for calculating the flux

To assess the optimal location of the point at which the derivatives should be calculated on the control volume face (see Figs. 1 and 2), the representative point was allowed to vary from the edge point R to the center point E as follows:

$$\mathbf{x}_F = (1 - \eta)\mathbf{x}_R + \eta\mathbf{x}_E \quad \text{for} \quad 0 \le \eta \le 1. \tag{15}$$

It should be noted that the derivatives must be estimated once on all edges of the mesh when $\eta = 0$, and once per element at the point E when $\eta = 1$.

When $0 < \eta < 1$, the derivatives must be estimated three times per element (once per control volume face or twice per edge). Clearly this option is the most expensive in terms of computational overhead, followed by the case $\eta = 0$. The least amount of work is associated with the case $\eta = 1$.

The acronyms shown in Table 1 were used to identify the different strategies implemented for the proposed control-volume finite-element least-squares flux approximation technique (*CVFE-LS*) and the performance of each scheme is reported in the next section.

3. Numerical Results

This section presents the numerical results obtained using the method described in the above sections for diffusion problems in near isotropic, orthotropic and anisotropic media. Different initial conditions and boundary conditions are used with the diffusion Eq. (1) to highlight the accuracy of the proposed method. Numerical solutions are compared with exact results when they are available. The physical values and functions used for each case are given in Table 1.

Tables 2, 3 and 4 provide a summary of the overall performance in terms of the number of *BiCGSTAB* iterations, computation time and errors (if available) for each case shown in Table 1 for different combinations of the method discussed in the previous sections. For the cases where exact solutions were available, the absolute maximum errors were provided in Tables 2 and 3. The results obtained by the *CVFE-LSe* methods on fine meshes were considered as the base result to compare with the results on very coarse meshes for the cases where exact solutions were unavailable and these results were compared graphically.

Physical values, parameters and acronyms

Parameter/Function(Units)	*Case 1*	*Case 2*	*Case 3*	*Case 4*	*Case 5*	*Case 6*
ϕ_s (^0C)	140	140	140	0	140	0
K $(W/m/K)$	K_1	K_2	K_3	K_3	K_4	K_5
$F(x,y)$ (^0C)	30	30	30	$30f$	30	$30f$

$$K_1 = \begin{bmatrix} 1.54 & 0 \\ 0 & 0.154 \end{bmatrix} \quad K_2 = \begin{bmatrix} 154 & 0 \\ 0 & 0.154 \end{bmatrix} \quad K_3 = \begin{bmatrix} 1540 & 0 \\ 0 & 0.154 \end{bmatrix}$$

$$K_4 = \begin{bmatrix} 0.462 & 0.308 \\ 0.308 & 0.462 \end{bmatrix} \quad K_5 = \begin{bmatrix} 152 & 18 \\ 18 & 2.5 \end{bmatrix} \quad f = e^{-5(x-3L/4)^2 - (y-M/2)^2}$$

$L = 0.1m \quad M = 0.04m \quad h = 10W/m^2/K$

$\delta t = 1s \quad T = 1000s \quad \gamma = 1.01316 \times 10^6 J/K/m^3$

Acronym	*CVFE-LSe2*	*CVFE-LSe3*	*CVFE-LSm2*	*CVFE-LSm3*
Parameter				
c	2	2	2	2
m	2	3	2	3
r	9	15	9	15
η	1.0	1.0	0.5	0.5

Table 1:

c - The parameter for the weight coefficients, w_j's in least squares technique

m - The parameter in Eq. (4), (7) and (12)

r - Number of closest neighbours used for estimating derivatives

η - The parameter in Eq. (15)

Summary of results for the cases 1, 2 and 3 on meshes (a) and (b)

	Mesh	(a)			(b)		
	Scheme	A.M.E.	T.I.	C.T.	A.M.E.	T.I.	C.T.
1	CVFE-LSe2	0.066	8751	24.1	0.287	4068	2.5
	CVFE-LSe3	0.081	8760	41.1	0.374	4053	5.0
	CVFE-LSm2	0.064	8750	117.2	0.247	4065	12.4
	CVFE-LSm3	0.065	8759	198.1	0.299	4055	17.9
	Hybrid	0.111	8746	6.5	0.636	4070	
2	CVFE-LSe2	0.030	75630	66.2	0.314	27746	4.5
	CVFE-LSe3	0.044	75984	84.9	0.421	27886	7.1
	CVFE-LSm2	$0.027^\$$	75591	70.2	0.621	27718	14.0
	CVFE-LSm3	$0.049^\%$	75790	236.4	0.500	27802	20.2
	Hybrid	10.710	75623	49.1	17.255	28307	2.7
3	CVFE-LSe2	0.061	244936	178.6	0.334	81784	9.5
	CVFE-LSe3	0.096	245393	190.6	0.587	82128	12.1
	CVFE-LSm2	$0.067^\$$	245639	180.8	0.636	81893	18.9
	CVFE-LSm3	$0.148^\%$	246613	350.3	0.696	82452	24.9
	Hybrid	10.713	233700	151.6	17.248	82947	7.8

Table 2:

Results on (a) fine mesh and (b) coarse mesh

A.M.E. - Absolute maximum error, C.T. - Computational time,

T.I - total number of $BiCGSTAB$ iterations

% - $c = 0$ is used in least squares technique, $ - $r = 15$ used instead of 10

Figs. 4-10 illustrate the exact and numerical results for some selected cases using the meshes generated using EasyMesh [26] shown in Fig. 4. Note that the control volumes are constructed around the vertices as shown in Fig. 1. One can see that the new *CVFE-LSe* method not

Summary of results for the cases 1, 2 and 3 on meshes (c) and (d)

	Mesh	(c)			(d)		
	Scheme	A.M.E.	T.I.	C.T.	A.M.E.	T.I.	C.T.
1	CVFE-LSe2	0.536	4000	1.0	0.8277	10278	3.9
	CVFE-LSe3	0.666	4000	1.9	0.8901	10267	7.8
	CVFE-LSm2	0.440	4000	5.7	0.6834	10267	15.3
	CVFE-LSm3	0.548	4000	8.6	0.9123	10288	24.1
	Hybrid	1.123	4000	0.2	3.0438	10212	1.3
2	CVFE-LSe2	0.408	18915	1.6	0.534	56499	9.0
	CVFE-LSe3	0.510	18892	2.4	0.705	56140	12.8
	CVFE-LSm2	0.573	18862	6.3	0.572	56837	19.7
	CVFE-LSm3	0.681	18895	9.2	0.862	56139	28.8
	Hybrid	16.750	18624	0.8	15.834	54120	5.9
3	CVFE-LSe2	0.333	51923	3.0	1.0666	99571	13.2
	CVFE-LSe3	0.440	51862	3.8	1.0124	101563	17.3
	CVFE-LSm2	0.474	51916	7.6	0.8092	99793	24.2
	CVFE-LSm3	0.652	51769	10.5	0.9362	99819	33.2
	Hybrid	16.808	51134	2.1	17.484	97962	10.5

Table 3:

Results on (c) very coarse mesh and (d) distorted mesh

A.M.E. - Absolute maximum error, C.T. - Computational time,

T.I - total number of $BiCGSTAB$ iterations

% - $c = 0$ is used in least squares technique, $ - $r = 15$ used instead of 10

Summary of results for the cases 4, 5 and 6

	Mesh	(a)		(b)		(c)		(d)	
	Scheme	T.I.	C.T.	T.I.	C.T.	T.I.	C.T.	T.I.	C.T.
4	CVFE-LSe2	244962	174.2	81722	9.5	51597	2.9	99945	13.2
	CVFE-LSe3	245028	190.4	82071	12.1	51765	3.9	101796	17.3
	Hybrid	232537	154.9	83325	7.7	51112	2.2	97804	10.5
5	CVFE-LSe2	6973	23.4	4000	2.5	3060	0.9	7804	3.6
	CVFE-LSe3	6972	38.3	4001	5.0	3062	1.8	7802	7.6
	Hybrid	6972	5.4	4001	0.5	3053	0.2	7788	1.0
6	CVFE-LSe2	76879	67.8	28655	4.7	18863	1.6	56392	8.7
	CVFE-LSe3	76194	82.2	28635	7.3	18987	2.5	56346	12.6
	Hybrid	75395	49.6	28926	2.8	19034	0.8	57219	6.4

Table 4:

Results on (a) fine mesh, (b) coarse mesh (c) very coarse mesh and (d) distorted mesh

C.T. - Computational time, T.I - total number of $BiCGSTAB$ iterations

only provides consistent results for all meshes tested but also is able to capture the underlying physics transpiring in the exact solution for a range of anisotropy ratios including extreme values. The previously documented hybrid $CVFE$ scheme is only able to capture the physics for near isotropic cases (see cases 1 and 5). Furthermore, the $CVFE\text{-}LSe2$ or $CVFE\text{-}LSe3$ schemes implemented on coarse meshes are both accurate and competitive in computation time (see Tables 2 and 3) in comparison with the hybrid method. In fact, one can obtain acceptable accuracy using the $CVFE\text{-}LSe$ schemes with less computation time than the hybrid method (see cases 1, 5 and 6). Note that the hybrid method failed to produce reasonable results for cases 2, 3, 4 and 6.
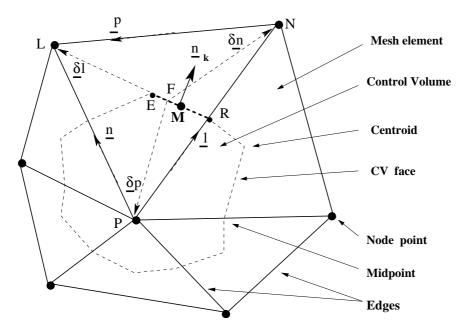
Figure 1: A typical control volume and vectors associated with a control volume face
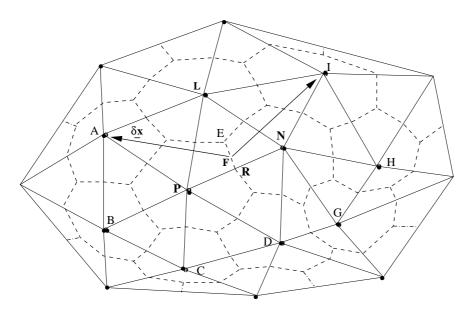
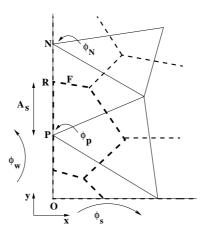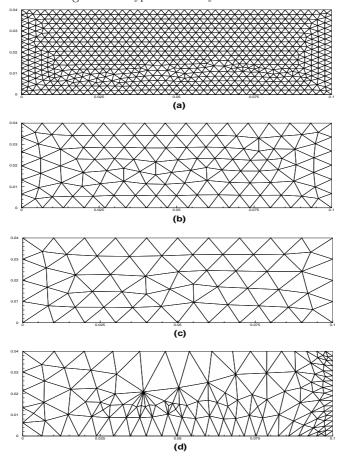Figure 2: A distribution of nodes considered for the flux approximation on a control volume face

Figure 3: A typical boundary control volume.

Figure 4: The meshes used for the numerical simulations: (a) fine mesh - 1504 elements   (b) coarse mesh - 218 elements (c) very coarse mesh - 106 elements and (d) distorted mesh - 237 elements

Figure 5: Comparison of results for *Case 1*. (a), (b), (c): exact solutions, (d), (e), (f): *CVFE-LSe*3, (g), (h), (i): Hybrid, Top row: on fine mesh, Middle row: on coarse mesh, Bottom row: on very coarse mesh
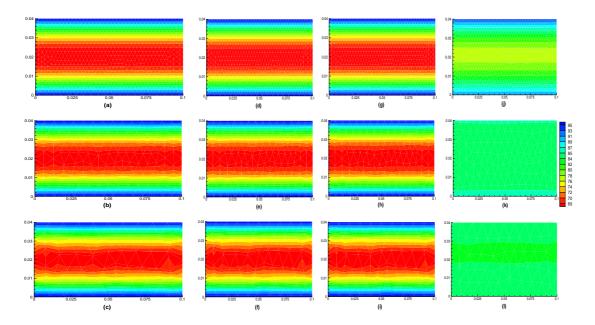

Figure 6: Comparison of results for *Case 3*. (a), (b), (c): exact solutions, (d), (e), (f): *CVFE-LSe*2, (g), (h), (i): *CVFE-LSe*3, (j), (k), (l): Hybrid, Top row: on fine mesh, Middle row: on coarse mesh, Bottom row: on very coarse mesh
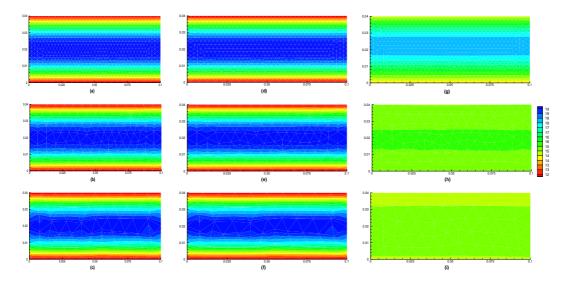
Figure 7: Comparison of results for *Case 4*. (a), (b), (c): *CVFE-LSe*2, (d), (e), (f): *CVFE-LSe*3, (g), (h), (i): Hybrid, Top row: on fine mesh, Middle row: on coarse mesh, Bottom row: on very coarse mesh
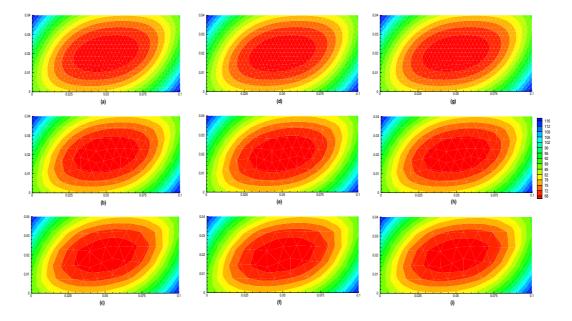

Figure 8: Comparison of results for *Case 5* (a), (b), (c): *CVFE-LSe*2, (d), (e), (f): *CVFE-LSe*3, (g), (h), (i): Hybrid, Top row: on fine mesh, Middle row: on coarse mesh, Bottom row: on very coarse mesh

Figure 9: Comparison of results for *Case 6* (a), (b), (c): *CVFE-LSe*2, (d), (e), (f): *CVFE-LSe*3, (g), (h), (i): Hybrid, Top row: on fine mesh, Middle row: on coarse mesh, Bottom row: on very coarse mesh
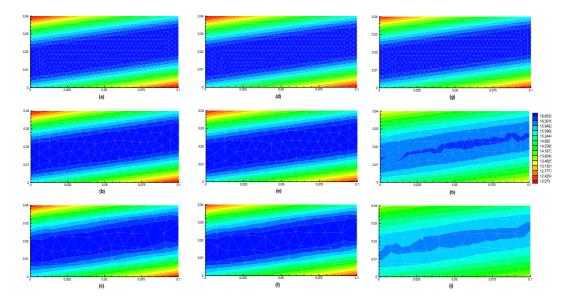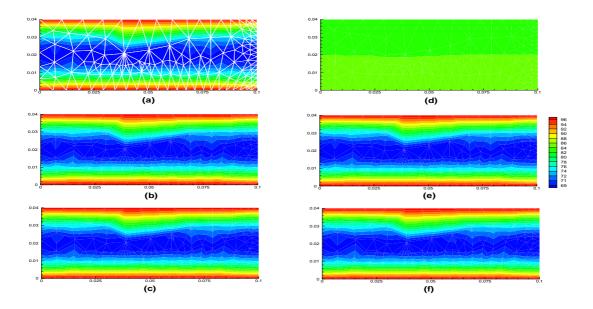

Figure 10: Comparison of results for *Case 3* on distorted mesh for each method considered: (a) Exact Solution and the mesh used, (b) *CVFE-LSe*2, (c) *CVFE-LSe*3, (d) Hybrid, (e) *CVFE-LSm*2, (f) *CVFE-LSm*3

The *CVFE-LSe* methods performed well for all cases whereas the *CVFE-LSm* methods succeeded only with some constraints for the cases with extreme anisotropy ratios on the fine mesh (see Table 3). For all other meshes both schemes provided consistent results, however, the *CVFE-LSe* schemes were the most accurate. One plausible explanation for this finding may be the use of a different set of neighbouring points for the *CVFE-LSm* method to estimate the derivatives for the correction term at each control volume face within the triangle. This fact will be investigated further in future research. Note that the *CVFE-LS3m* methods worked for the fine mesh only when no weighting was used in the least squares method for the extreme anisotropy cases.

The use of the *CVFE-LSe* methods on very coarse meshes was successful for every case and the computational time was low. While the hybrid method converges faster than the *CVFE-LS* methods, which has additional computational overheads in order to estimate the derivatives of the function, the accuracy of the results produced by the hybrid method is very poor. It is worthwhile to note that the computational time (see Tables 2, 3 and 4) for the hybrid method, which provides reasonably accurate results on the fine mesh, is much higher than the computational time taken by the *CVFE-LS* methods, which has a high accuracy on very coarse meshes.

Table 2, 3 and 4 also depict that the hybrid method and the *CVFE-LS* methods have a similar order of BiCGSTAB iterations. This is due the fact that the system matrix L in Eq. (10) is the same for every method including the hybrid method, and there are only small variations in the total number of iterations due to the presence of the correction term $\underline{\epsilon}$ in the right hand side of the Eq. (10) for the *CVFE-LS* methods.

Finally, all of the *CVFE-LS* schemes and the hybrid method were tested on the distorted mesh (see Fig. 4d) for all the cases shown in Table 1. However, more neighbouring points were required to estimate the derivatives at the control volume faces for this mesh (i.e., 15 and 25 closest neighbouring points for the *CVFE-LS2* and *CVFE-LS3* schemes respectively). The increase of computational times and *BiCGSTAB* iterations (refer column (d) of Tables 3 and 4) for each method on the distorted mesh reflects the use of additional neighbouring points and the impact on the condition of the matrix L (see Eq. (10)) due to the poor quality of the mesh (i.e., geometrical properties). Fig. 10 shows the results for case 3 on mesh (d) where the hybrid technique again failed to capture the physics of the problem with a strong anisotropy. Due to the poor quality of this mesh and the interpolation technique used by the plotting software, the true symmetry of the solution is slightly concealed in these figures. One can notice that the hybrid method has failed to produce good results for case 1 (near isotropic case) also on this distorted mesh (see Table 3 column (d)). These results give further evidence that the newly proposed *CVFE-LS* method is capable of providing acceptable results for a wide class of transport problems with high anisotropy ratios on both good and bad meshes.

4. Conclusions

The key feature of the *CVFE-LSe* methods is that these techniques provide accurate and similar results on every mesh for each case investigated. Although these methods need more computational time than the hybrid (*CVFE*) scheme for the same mesh size due to the fact that the derivatives of the function required for the flux correction term were estimated using the least squares technique for each element in the mesh, they do provide consistent and accurate results. However, this computational overhead is compensated by the fact that the new scheme provides consistent and accurate results on coarse meshes where the computational time becomes very competitive, if not superior, with the hybrid scheme implemented on fine meshes. These findings are a very important contribution of the newly introduced flux approximation technique.

This work also shows a number of weaknesses in the hybrid (*CVFE*) technique as pointed out by authors elsewhere [9, 13]. Firstly the inaccuracy of the hybrid technique in simulating

transport problems in highly anisotropic media, for examples, see Figs. 6, 7 and 9. Secondly the hybrid methods need very fine meshes to produce accurate results, which increases the computational time, for example see the results shown in Fig. 9 and the comparison of the computational time for case 6 shown in Table 4.

In conclusion the *CVFE-LSe* method is highly recommended for simulating anisotropic diffusion problems implemented on both structured and unstructured meshes, and this method supersedes the previously published hybrid *CVFE* scheme.

References

[1] S.V. Patankar, Numerical Heat Transfer and Fluid Flow, Hemisphere Publishing Corporation, 1980.

[2] J. Russell Manson and Steve G. Wallis, Accuracy Characteristics of Traditional Finite Volume Discretizations for Unsteady Computational Fluid Dynamics, *Journal of Computational Physics*, **132** (1997), 149.

[3] F. Hermeline, A Finite Volume Method for the Approximation of Diffusion Operators on Distorted Meshes, *Journal of Computational Physics*, **160** (2000), 481.

[4] William A. Wood and William L. Kleb, Diffusion Characteristics of Finite Volume and Fluctuation Splitting Schemes, *Journal of Computational Physics*, **153** (1999), 353.

[5] I. Aavatsmark, T. Barkve, Ø. Bøe and T. Mannseth, Discretization on Unstructured Grids for Inhomogeneous, Anisotropic Media. Part I: Derivation of the Methods, *SIAM J. Sci. Compt.*, **19**:5 (1998), 1700.

[6] I. Aavatsmark, T. Barkve, Ø. Bøe and T. Mannseth, Discretization on Unstructured Grids for Inhomogeneous, Anisotropic Media. Part II: Discussion and Results, *SIAM J. Sci. Compt.*, **19**:5 (1998), 1717.

[7] W.J. Ferguson and I. W. Turner, A Control Volume Finite Element Numerical Simulation of the Drying of Spruce, *Journal of Computational Physics*, **125** (1996), 59.

[8] I. Aavatsmark, T. Barkve, Ø. Bøe and T. Mannseth, Discretization on Non-Orthogonal, Quadrilateral Grids for Inhomogeneous, Anisotropic Media, *Journal of Computational Physics*, **127** (1998), 2.

[9] P.A. Jayantha and I.W. Turner, A Comparison of Gradient Approximations for use in Finite Volume Computational Models for Two-Dimensional Diffusion Equations, *Numerical Heat Transfer, Part B: Fundamentals*, **40**:5 (2001), 367.

[10] P.A. Forsyth, A Control Volume Finite Element Approach to NAPL Groundwater Contamination, *SIAM J. Sci. Stat. Comput.*, **12**:5 (1991), 1029.

[11] L.S.K Fung, L. Buchman and R. Sharma, Hybrid-CVFE Method for Flexible-Grid Reservoir Simulation, *SPE Reservoir Engineering*, **9**:3 (1994), 188.

[12] P. Perré. and I. Turner, TransPore: A Generic Heat and Mass Transfer Computational Model for Understanding and Visualising The Drying Of Porous Media, Invited paper, *Drying Technology Journal*, **17**:7, (1999), 1273.

[13] P.A. Jayantha and I.W. Turner, Generalised Finite Volume Strategies for Simulating Transport in Strongly Orthotropic Porous Media, *Australian & New Zealand Industrial and Applied Mathematics Journal*, **44**:E (2003), C1–C21.

[14] P.A. Jayantha and I.W. Turner, A Second Order Finite Volume Technique for Simulating Transport in Anisotropic Media, *The International Journal of Numerical Methods for Heat & Fluid Flow*, **13**:1 (2003), 31–56.

[15] P. Perré., I. Turner and J. Passard, 2-D Solution for Drying with Internal Vaporization of Anisotropic Media, *AIChE Journal*, **45**:1 (1999), 13.

[16] F.M.L. Traiano, R.M. Cotta and H.R.B. Orlande, Improved Approximate Formulations for Anisotropic Heat Conduction, *Int. Comm. Heat Mass Transfer*, **24**:6 (1997), 869.

[17] S. Ghorai, A.S. Tomlin and M. Berzins, Resolution of Pollutant Concentrations in the Boundary layer using a Fully 3D Adaptive Gridding Technique, *Atmospheric Environment*, **34** (2000), 2851.

[18] H. Kazeminejad, Numerical Analysis of Two Dimensional Parallel Flow Flat-Plate Solar Collector, *Renewable Energy*, **26** (2002), 309.

[19] I.W. Turner, J.R. Puiggali and W. Jomaa, A Numerical Investigation of Combined Microwave and Convective Drying of a Hygroscopic Porous Material: A Study Based on Pine Wood, *Trans IChemE*, **76**:Part A (1998), 193.

[20] M.F. Abdul Azeez and A.F. Vakakis, Axisymmetric Transient Solutions of the Heat Diffusion Problem in Layered Composite Media, *International Journal of Heat and Mass Transfer*, **43** (2000), 3883.

[21] J. Fainberg and H.-J. Leister, Finite Volume Multigrid Solver for Thermo-Elastic Stress Analysis in Anisotropic Materials, *Computer Methods in Applied Mechanics and Engineering*, **137** (1996), 167.

[22] E. Turkel, Accuracy of Schemes with Nonuniform Meshes for Compressible Fluid Flows, Institute for Computer Applications in Science and Engineering, Report No. 85-43, National Aeronautics Space Administration, Virginia, 1985.

[23] T.J. Barth, Aspects of Unstructured Grids and Finite-Volume Solvers for the Euler and Navier-Stokes Equations, in: Lecture Notes Presented at the VKI Lecture Series 1994-05.

[24] C. Ilinca, X.D. Zhang, J.-Y. Trépanier and R. Camarero, A Comparison of Three Error Estimation Techniques for Finite-Volume Solutions of Compressible Flows, *Computer Methods in Applied Mechanics and Engineering*, **189** (2000) 1277.

[25] C.F. Ollivier-Gooch, A New Class of ENO Schemes Based on Unlimited Data-Dependent Least-Squares Reconstruction, in: AIAA - 34th Aerospace Sciences Meeting and Exhibit, Reno, NV, US, AIAA-96-0887, 1996.

[26] Niceno, B., "EasyMesh" (Version 1.4), freely available mesh generator on the web Site: `http://www-dinma.univ.trieste.it/~nirftc/research/easymesh/`.